Article

Combined Effects of Sulfate and Chloride Attack on Steel Reinforced Mortar under Drying–Immersion Cycles

Hongfang Sun [1], Hao Zou [1], Xinwei Li [1], Shazim Ali Memon [2], Binyang Yuan [1], Feng Xing [1], Xiaogang Zhang [1,*] and Jie Ren [1,3,*]

[1] Guangdong Provincial Key Laboratory of Durability for Marine Civil Engineering, College of Civil and Transportation Engineering, Shenzhen University, Shenzhen 518060, China

[2] Department of Civil Engineering and Environmental Engineering, School of Engineering and Digital Sciences, Nazarbayev University, Astana 010000, Kazakhstan

[3] Department of Civil, Environmental, and Architectural Engineering, 1111 Engineering Drive, UCB 428, University of Colorado Boulder, Boulder, CO 80309, USA

* Correspondence: szzxg@szu.edu.cn (X.Z.); jie.ren@colorado.edu (J.R.)

Abstract: In this study, X-ray microcomputed tomography (XCT) and nanoindentation techniques were used to evaluate the synergistic action between sulfate and chloride ingress under cyclic drying–immersion conditions on steel-reinforced mortars. Three salt solutions, namely 3% NaCl (Sc), 5% Na_2SO_4 (Ss), and 5% Na_2SO_4 + 3% NaCl (Scs), were used and 24 drying–immersion cycles were applied. The results showed that the chloride caused more severe corrosion on steel reinforcement than the sulfate while under the influence of Scs, and the presence of sulfate suppressed the steel corrosion caused by chloride. In terms the damage to the mortar cover, after 24 drying–immersion cycles, the sulfate caused the most severe damage (volume loss of approximately 7.1%) while the chloride resulted in the least damage (volume loss of approximately 2.6%). By comparing Ss and Scs, it was also found that chloride suppressed the sulfate attack by reducing the damage to the mortar cover (volume loss of approximately 6.3% for Scs). Moreover, the degradation of mortar specimens was found to be layer-dependent, as was the distribution of micro-mechanics. Regarding the micro-mechanics, the specimens of the three solutions performed differently in terms of the aforementioned properties, depending on which underlying mechanism was analyzed. This research could allow for a more accurate assessment of the factors influencing building structures in a typical aggressive marine environment.

Keywords: Portland cement mortar; sulfate; chloride; drying–immersion cycle; XCT; nanoindentation

1. Introduction

The durability of reinforced concrete-based structures is crucial in the field of civil engineering. In marine environments, the coexistence of chloride and sulfate has become one of the major causes of the deterioration of reinforced concrete-based structures [1]. It is widely known that chloride ingress mainly results in severe corrosion of steel reinforcement [2–4], while sulfate attack mainly induces damage to concrete cover [5,6]. When reinforced concrete structures are subjected to the synergistic impact of chloride and sulfate, the penetration rate of chloride ions may be accelerated, since the sulfate ions could cause damage to the concrete cover. This theory is supported by the results and conclusions of previous research [2,7]. However, other researchers have proposed an alternative explanation: that chloride and sulfate ions had a competitive relationship when they coexisted in concrete, which enhanced the resistance of reinforced concrete to chloride-induced corrosion [8–10]. Moreover, the conclusions regarding the effect of sulfate attack with the existence of chloride on concrete cover are controversial. Some researchers found that chloride slowed the diffusion of sulfate and inhibited sulfate attack by delaying the formation of ettringite and gypsum [11,12], while other researchers found that chloride ions

actually weakened the concrete's resistance to sulfate and accelerated sulfate attacks [13,14]. Therefore, it is important to further investigate the interaction between chloride and sulfate and their influence on reinforced concrete.

One potential reason for the conflicting conclusions in the literature may be the improper testing of the properties of reinforced concrete structures. As reported in several studies, the degradation level of concrete was usually characterized based on the mass loss (or dynamic modulus of elasticity) and macro-strength variations [15–18]. However, the specimens could adsorb liquids from the surrounding solutions during testing, which might have influenced measurement of the damage level for different cementitious materials. Similarly, for macro-mechanical properties, the area of contact region, or cross-section, was often used for the determination of mechanical strengths [19]. However, the volume loss of the specimen due to sulfate attack might influence the accuracy of the area measurement. Thus, a more accurate characterization of the degradation level of reinforced concrete is required in order to improve the evaluation of damage levels caused by external hazardous ions, such as sulfate and chloride.

X-ray computed tomography (XCT), a non-destructive technique that enables in situ monitoring of chemical compositions and morphologies of materials on a three dimensional scale, has been introduced to characterize the corrosion of rebars and cracking of covers in chloride-rich environments [20–22]. However, to the best knowledge of the authors, the application of XCT in evaluating the degradation of cementitious cover under the combined influence of chloride and sulfate coupled with drying–immersion cycles, which are more aggressive compared to normal immersion, has not yet been studied. Most reinforced concrete structures experience multiple deteriorating actions simultaneously throughout their entire service lives, and the combination of these forces could sometimes be more detrimental than any single deterioration process alone [16,17]. Therefore, it is important to study the degradation of reinforced cementitious materials under a combination of typical deteriorating actions with possible synergistic effects.

Regarding the accurate evaluation of mechanical properties for concrete cover, nanoindentation is an applicable method for properly assessing the mechanical properties of cement-based materials [23,24]. However, traditional nanoindentation testing is normally performed with optical microscopes. Due to the observational limit of optical microscopes (sub-micro resolution with no chemical composition information), researchers had to combine statistical analyses to determine the micro-mechanical properties of each phase in hydrated cementitious materials [25]. Thus, more time and effort were dedicated to data analysis, which could affect the accuracy of results. This issue can be largely avoided by using in situ nanoindentation, which combines real-time SEM–BSE imaging with on-site nanoindentation. This approach allows researchers to easily and accurately acquire the micro-mechanics of a known phase such as C-S-H during the indenting process [26,27] and is a very powerful tool to evaluate the degradation of cement paste in this study.

Therefore, we used a non-destructive XCT technique to evaluate the degradation of reinforced mortars under the combined influence of chloride and sulfate under a drying–immersion cyclic condition. The employed drying–immersion condition was to mimic the periodic splashing in coastal environments, which is normally more aggressive compared to a full immersion condition [28–32]. In addition, an in situ nanoindentation technique coupled with SEM–BSE was introduced to characterize the degradation profiles of specimens exposed to formulated salt solutions. This research offers to a more accurate assessment of the factors influencing the durability of building structures in marine conditions or similar environments rich in chlorides and sulfates.

2. Materials and Methods

2.1. Materials and Specimen Preparation

In this study, cylindrical mortar specimens with a diameter of 10 mm and a height of 40 mm were prepared. An embedded steel rod with a diameter of 3 mm and length of 45 mm was placed in the center of mortar as shown in Figure 1. The steel rod used

was Q235, which meets the requirement of Chinese standard GB/T3274-2007 [33], and its chemical composition is shown in Table 1. For the preparation of mortars, Portland cement was used and its chemical composition is shown in Table 2. The fine aggregates used met the requirements of Chinese standard GB/T17671-1999 (equivalent to ISO 679: 1989) [34] and the particles larger than 300 μm were removed. The water-to-cement ratio was 0.4 and the cement-to-sand ratio was 1:1. Based on this mix proportion, at first, the cement and aggregate were dry-mixed for 2 min to ensure homogeneity of the solid raw materials. Water was then added, and the mixture was mixed for additional 4 min. After placing the mixture into molds, the molds were sealed and kept in a curing chamber (95 ± 5% RH, 20 ± 2 °C) for 48 h. Thereafter, the specimens were demolded and kept in the curing chamber for a total curing period of 28 days. The part of the steel rod exposed to the air was coated with an epoxy resin to avoid the corrosion of uncovered steel during the curing period and further testing.
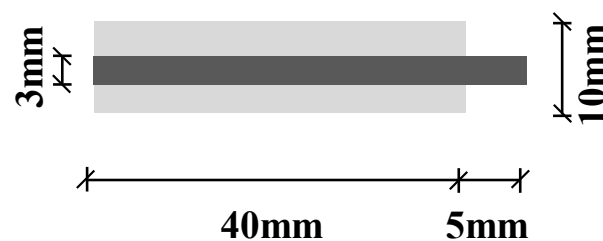

Figure 1. A schematic presentation of a specimen.

Table 1. Chemical composition of the Q235 steel used in the study.

Element	C	Si	Mn	P	S	N	Cr	Cu	Ni	Fe
Mass fraction	0.09	0.03	0.42	0.02	0.02	0.005	≤0.02	0.04	≤0.3	Bal.

Table 2. Chemical composition of the Portland cement used in this study.

Oxides.	Content (wt.%)
SiO_2	21.20
Al_2O_3	5.40
Fe_2O_3	5.03
CaO	64.84
MgO	1.45
SO_3	1.02
LOI	1.06

2.2. Setting of Drying–Immersion Cycles

After 28 days of curing, the mortar specimens were subject to drying–immersion cycles. A schematic diagram of the test is shown in Figure 2.

The drying–immersion cycle consisted of two days of wetting followed by five days of drying (seven days in total). During the wetting period, the specimens were immersed in 3 wt.% NaCl solution (specimen Sc), 5 wt.% Na_2SO_4 solution (specimen Ss), or a mixture of 3 wt.% NaCl and 5 wt.% Na_2SO_4 solution (specimen Scs), respectively. The selected concentration of NaCl and Na_2SO_4 was in accordance with ASTM C1202 and ASTM C1012, respectively. During the drying period, the specimens were placed in a chamber maintained at a relative humidity (RH) of 20 ± 5% and temperature of 50 ± 1 °C. In total, the specimens were subject to 24 drying–immersion cycles and the overall test lasted for 168 days.
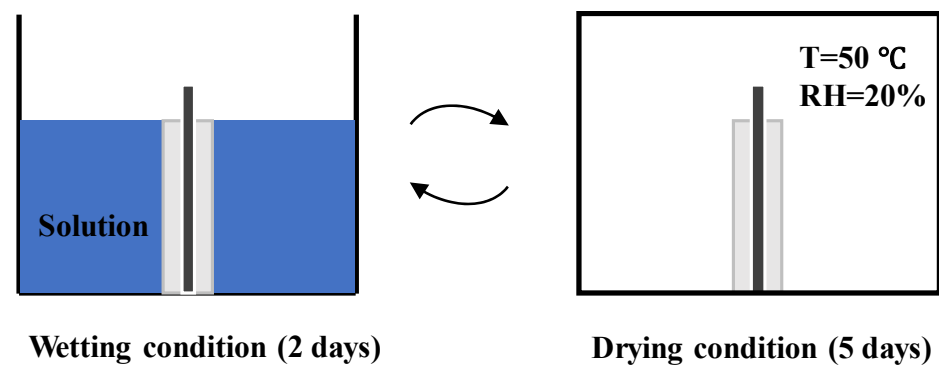
Figure 2. Schematic diagram of the drying–immersion cycles employed in this study.

2.3. Testing

2.3.1. XCT Testing

After different drying–immersion cycles (0, 6, 12, and 24), the specimens were scanned with Micro-XCT-400 (Zeiss, Oberkochen, Germany) equipment. The XCT system consists of a microfocus X-ray emitter, a rotation stage that allows for capturing of images in 360 degrees, an image-intensifier detector with three multiple charge-coupled device (CCD) cameras, and an image processing unit (see Figure 3). During the test, the sample was placed on the rotation stage between an X-ray emitter and a detector. The X-rays emitted penetrated through the sample and were received by the detector to generate a 2D projection image. During the scanning process, the stage rotated 360 degrees cumulatively at a certain rate around the vertical axis and a series of 2D projection images were obtained, which were reconstructed into 3D image data using a 3D reconstruction software available with the equipment. The reconstructed images were shown as different gray-values, which reflected attenuation levels of X-rays passing through different components of the sample. The components (such as mortar and steel rod) were segmented based on attenuation level using the 3D reconstruction software.
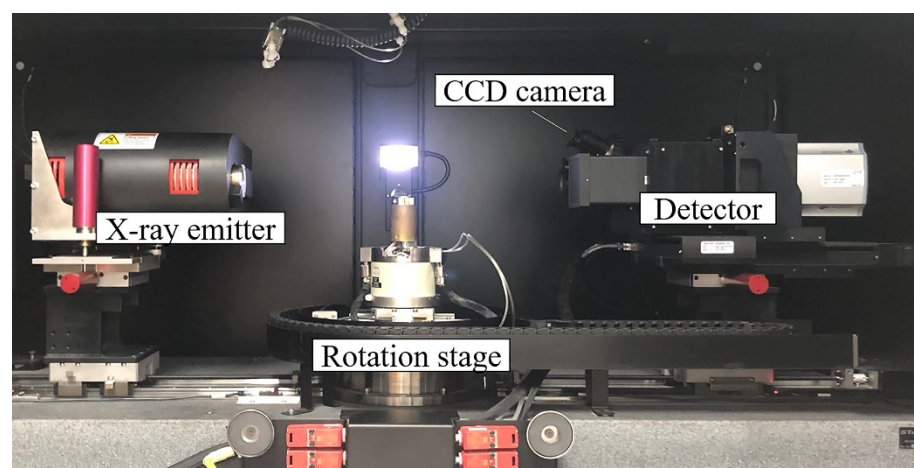

Figure 3. Internal features of Micro XCT-400 (Zeiss).

Two lenses, 0.4× and 4×, with resolutions of 11 μm and 4 μm, respectively, were used. During the testing, a voltage of 120 kV and a current of 82 μA were applied. The field of view (FOV) was 50 mm with an exposure time of 5 s. A total of 1,001 projection images were collected for each mortar specimen. After obtaining the reconstructed slice series, the components (mortar and steel rod) were segmented and quantitatively analyzed using the 3D reconstruction software. This software can combine 2D sliced images and extract statistical information including areas and volumes of segmented images. Then, the 3D information of the microstructure of specimens can be provided.

2.3.2. BSE-SEM

The samples used for the SEM test included those exposed to three drying–immersion cycle conditions: Sc, Ss, and Scs. Dried samples were immersed in epoxy resin, and after the resin hardened, samples were cut with a low-speed diamond saw to expose the fresh internal cross-section. Samples were then polished with abrasive paper of progressively smaller sizes (9, 6, 3, 1, and 0.25 µm). After that, polished samples were cleaned in an ultrasonic bath, using ethanol after each polishing. Finally, the observation surface of sample was coated with a gold film in vacuum mode to mitigate charging effects and increase corresponding electrical conductivity for a better observation [35]. In this study, the BSE mode was used to study the microstructure of the polished part. This analysis was carried out with field emission environment scanning electron microscopy (The FEI Quanta FEG 250, The Netherlands).

2.3.3. Nanoindentation in SEM

A nanoindentation manipulator (PI 85L SEM PicoIndenter, Hysitron) in the SEM chamber was used to investigate the micro-mechanical behavior of mortars subjected to the wetting and drying cycles. The manipulator in SEM is mainly composed of sample and probe stages. Piezoelectric inertial drives of the manipulator enabled long-range and fine-range motions in the X, Y, and Z directions. The fine motion of the manipulator provided a continuous movement of the sample with 0.02 nm resolution. It was then possible to indent a sample with a probe, simultaneously measuring the load by strain gauges. The load increment was 3 mN and the maximum load was 30 mN. To avoid being affected by surface roughness while testing, the nanoindentation was pushed to a depth of 1000 nanometers. During the testing, the nanoindenter acted mainly on the hydration products of cement, and possible influence of the unhydrated Portland cement and sand particles on the test results was carefully avoided. This is because these components hardly interact with chlorides and/or sulfates; hence, the results obtained from these components could result in misleading conclusions.

3. Results and Discussion

3.1. Influence on Steel Reinforcement

In order to examine the influences of different solutions (Sc, Ss and Scs) on steel reinforcement, 2D slices from the same location in cylindrical specimens were extracted for XCT analysis. The results of XCT after different drying–immersion cycles and immersion in three solutions (Sc, Ss, and Scs) are shown in Figure 4. The slices showed no significant corrosion of steel in all specimens, which indicated that the corrosion of steel was very mild during the testing cycles and was beyond the observational capacity of the XCT due to its resolution limit (approximately 11 µm).

However, the corrosion level of steel reinforcement could be determined by the color of the mortar surface after 24 drying–immersion cycles. As shown in Figure 5, compared to the specimens before exposure, the color of Sc after 24 drying–immersion cycles became dark brown, while the color of Ss was light brown. For Scs, it was somewhere between dark and light brown. The brown color of mortar cover of Sc is due to the seepage of corrosion products of steel reinforcement onto the surface. The color difference between the three specimens indicated that the corrosion level was higher in Sc while it was lower in Ss. Hence, chloride caused the most severe steel corrosion, while the specimen immersed in sulfate showed the least steel corrosion, although it was still visible. It can also be concluded from Scs, with a color in between dark and light brown, that sulfate hindered the steel corrosion caused by chlorides when they coexisted. This result corresponds well to a finding reported in another paper [9], that the combined exposure towards chloride and sulfate hindered the penetration of both ions.
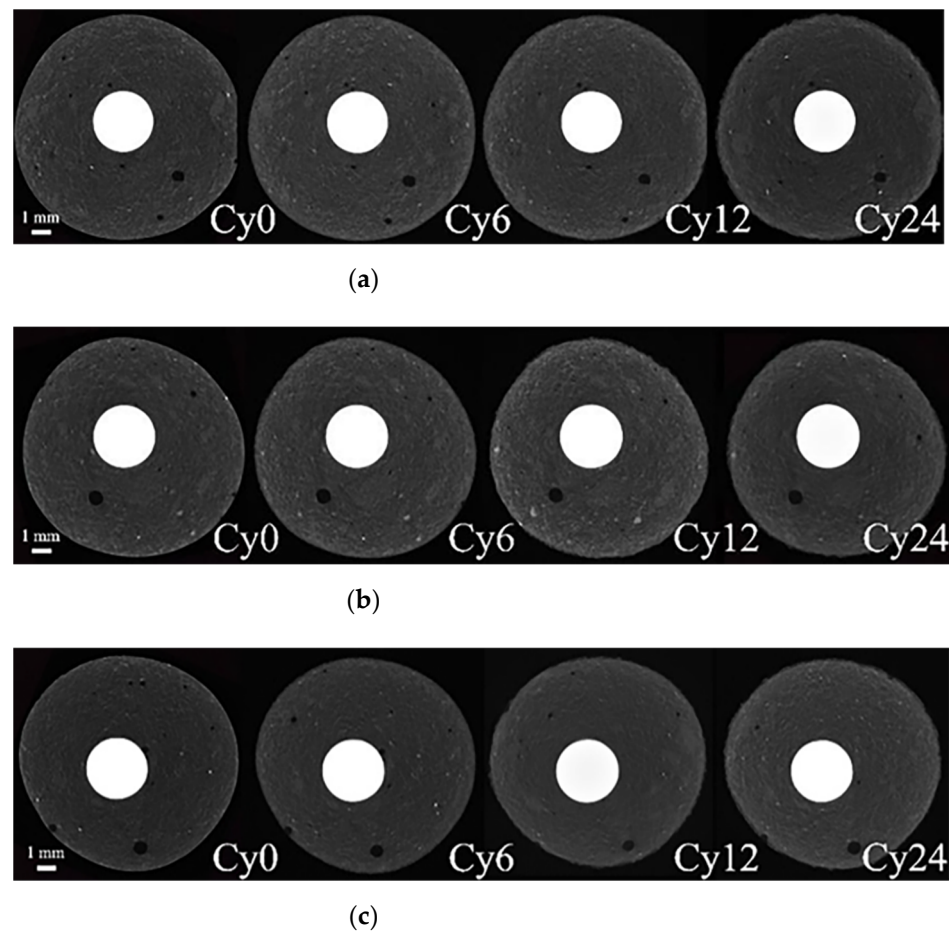
(**a**)

(**b**)

(**c**)

Figure 4. 2D slices from XCT results of specimens after different drying–immersion cycles: (**a**) Sc; (**b**) Ss, and (**c**) Scs.
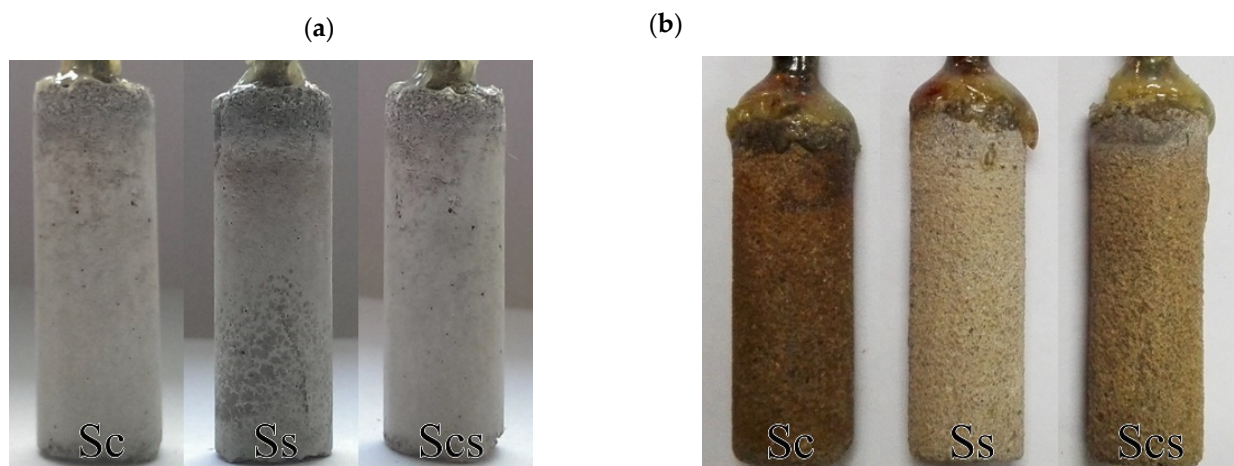

Figure 5. Mortar surface before and after drying–immersion cycle test: (**a**) Specimens before drying–immersion test; (**b**) specimens after 24 cyclic drying–immersion test. Sc to Scs (from left to right).

3.2. Influence on Mortar Cover

3.2.1. Qualitative Analysis

The influence of different salt solutions containing various amount of aggressive ions on mortar cover was also studied by XCT, and the results are presented in Figures 4–6. After 24 drying–immersion cycles, no visible cracks were observed in the mortar cover under XCT. However, the steel rust formed may still have flowed out through micro-cracks

with sizes smaller than the XCT resolution (~11 μm) or through diffusion [36] from small pores, as observed in Figure 5.

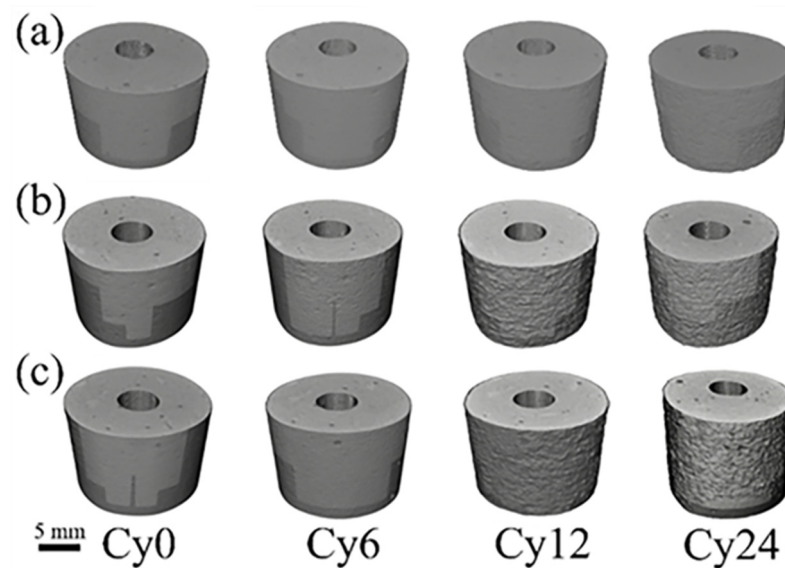**Figure 6.** Reconstructed 3D image of the three specimens after different drying–immersion cycles: (**a**) Sc; (**b**) Ss; (**c**) Scs.

It can also be seen from Figure 4 that the edge of the mortar gradually became blurred, indicating that the roughness of the mortar surface increased. The pictures shown in Figure 5 as well the XCT results presented in Figure 6 show this clearly. These results suggest that the specimens immersed in three solutions could cause degradation of mortar covers to varying extents. Throughout the entire test, the surface roughness of Sc was always much lower than that of Scs and Ss. This indicated that the NaCl solution resulted in the slightest deterioration on the mortar cover compared the Na_2SO_4 solution and the combined solution, because without the presence of sulfate, there was no formation of ettringite, which could lead to a volume expansion and resultant cracks. For Ss and Scs, the roughness of the surfaces were not notably different when observed through visual inspection after each cycle. Therefore, quantitative analysis was performed (Section 3.2.2) for more detailed investigations.

In order to investigate the surface roughness of the mortars, the specimens were cut after 24 cycles and observed using the XCT equipment with a 4× lens. The results are shown in Figure 7. It can be seen that the spalling of the cement paste matrix caused the rough surface, and as a result, the sand particles were exposed (indicated by white arrows) on the surface. In a more severe deterioration (Ss and Scs) condition, the falling-off of sand particles and pits were observed (indicated by black arrows) due to the lessened binding capacity of the cement paste. In order to quantify the degree of deterioration of the specimens, the volume loss ratios of all specimens in the three different solutions were compared and are discussed in the next section.

3.2.2. Quantitative Analysis

The volume loss ratios of the specimens immersed in three different solutions were calculated and plotted, as shown in Figure 8. It can be seen that the volume loss ratios of the specimens increased with the number of drying–immersion cycles. At the end of the 24th drying–immersion cycle, the volume losses of Sc, Ss, and Scs solutions were approximately 2.6%, 7.1%, and 6.3%, respectively. After each drying–immersion cycle, the volume loss of Ss was consistently the highest, while Sc had the smallest volume loss. This suggested that sulfate caused much more damage to the mortar cover than did chloride. By comparing the volume loss caused by Ss and Scs, the existence of chloride seems to suppress the sulfate

attack by approximately 11.3% after 24 cycles. As previously mentioned, this could be explained by the competitive antagonism effect between the two ions [9]. Another possible reason is that the formation of new stable products due to the ingress of chloride and sulfate densified the internal microstructure, leading to a slower rate of ionic diffusion [9,10]. It is also worth noting that the difference between the volume loss ratios of Ss and Sc became greater over time, indicating that the sulfate would ultimately cause much more severe damage to mortars than the chloride would.
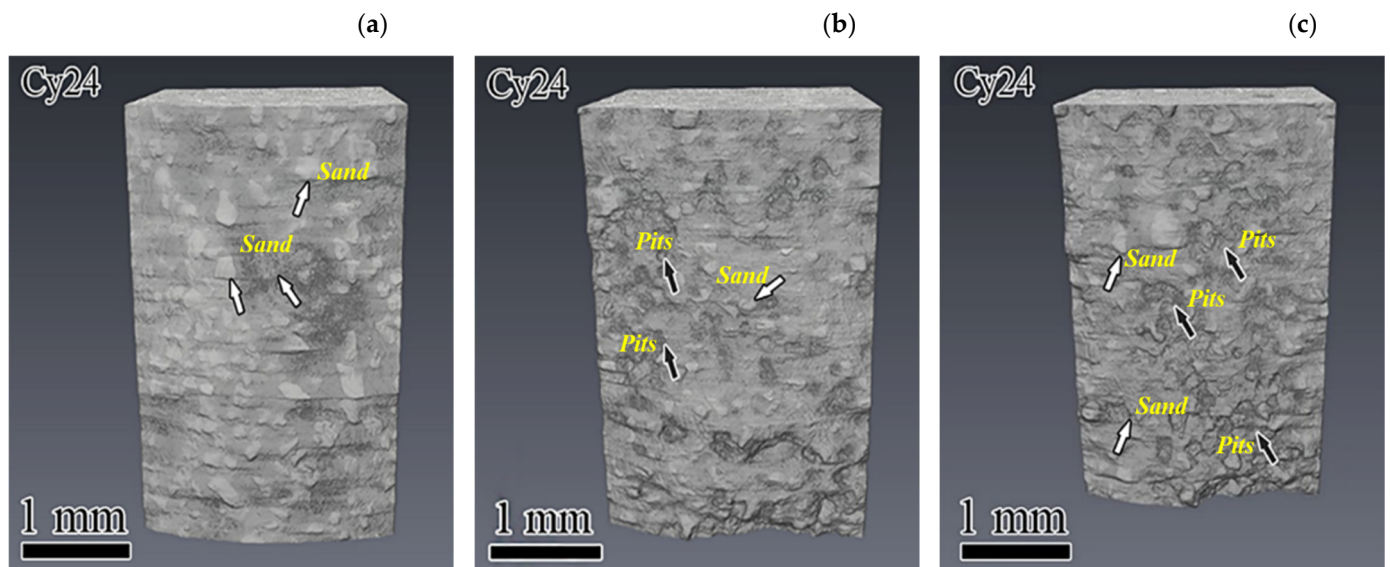

Figure 7. Reconstructed 3D image of the three specimens after 24 cycles: (**a**) Sc; (**b**) Ss; (**c**) Scs.
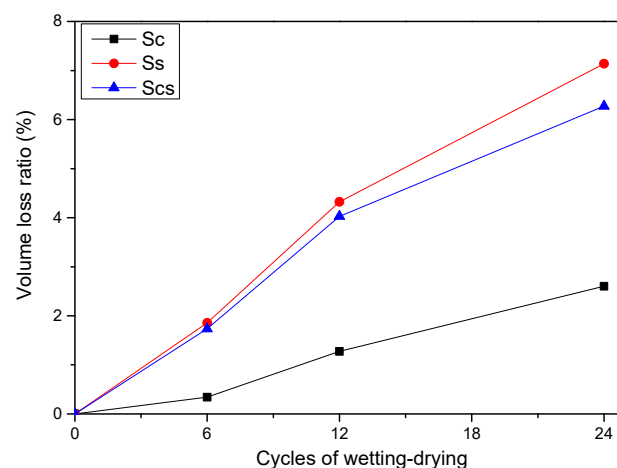

Figure 8. Volume loss ratio of the three specimens after 24 cycles.

3.2.3. Micro-Mechanic Analysis

The SEM–BSE technique was used to study the microstructure of the mortar protective layer degraded by drying–immersion cycles of samples exposed to the three salt solutions. The BSE images of the mortar cover after 24 drying–immersion cycles are shown in Figure 9. Three distinct layers were formed from the surface inwards, namely the surface layer, middle layer, and inner layer (separated by dotted lines in Figure 9). These layers were delineated by grayscale and intrinsic microstructures. The surface layer had the lowest grayscale due to its highest porosity. However, the porosity, or cracks, could not be observed since they were filled with an epoxy resin during the sample preparation process. In this layer, leaching of Ca mainly occurred [32], and the remaining composition gradually lost

the adhesion to sands. The middle layer showed the most compact feature due to the formation of more expansive gypsum, which contributed to a lower porosity. The inner layer had a microstructure similar to the part that remained uncorroded, although crack maps were observed, which were originated from the drying shrinkage caused by drying-immersion cycles. More details on the layer features and mechanisms can be found in a previous study [32]. It is worth noting that during the drying-immersion cycles, calcite could have been formed in the surface and middle layer of the specimens owing to the carbonation effect [32,37].
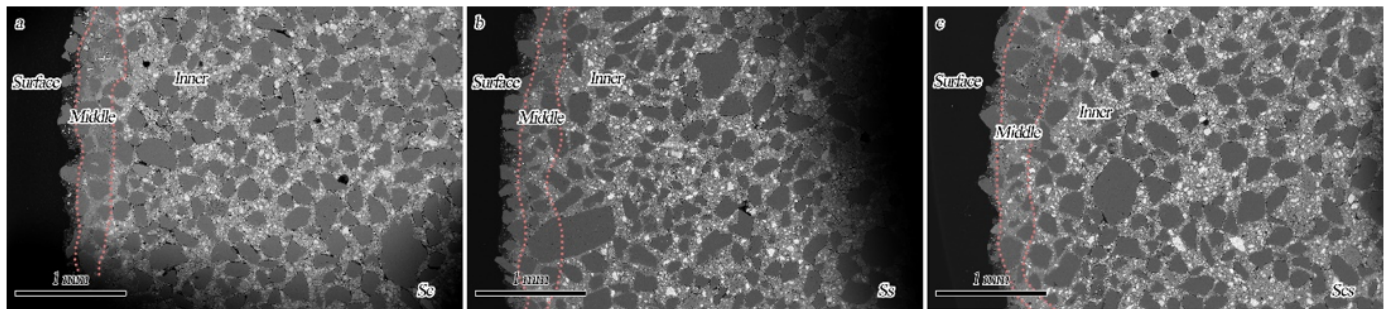

Figure 9. Microscopic BSE images of specimens after drying–immersion cycles in the three erosive salt environments: (**a**) Sc; (**b**) Ss; (**c**) Scs.

In order to determine the micro-mechanics of the three layers in mortars, nanoindentation was performed along with the SEM–BSE analysis. A typical BSE image of the indent on the surface of mortar is shown in Figure 10a, while a load–displacement curve at a certain site is shown in Figure 10b. During the tests, the load–displacement process lasted for 50 s. The loading time was 30 s while the unloading time was 20 s. The maximum load was adopted for each site to reflect the micro-mechanical properties of mortars. Then, the maximum load of each layer of mortars with a step of approximately 50 μm was recorded, and the results are presented in Figure 11. The indentation was performed at the region of C-S-H gel since it was the part that could be affected by external solutions. During the testing, the unhydrated Portland cement and sand particles could be avoided to a large extent, since the grayscale of C-S-H gels can be easily distinguished.

From Figure 11, it can be seen that the three specimens showed different mechanical properties. The load in the surface layer of the three specimens started from 2.2–2.5 mN, where the pores of the layer were filled by the hardened epoxy resin. The value of this layer is the lowest among the three layers due to the worsened binding capacity associated with the leaching and decalcification phenomenon. Therefore, the sand particles were found detached from the surface of the specimens, as illustrated in Figure 7. The load then increased slowly until reaching the middle layer, where the load rose rapidly from 2.2–2.7 mN to a peak of approximately 12.5 mN, 9.6 mN, and 6.3 mN for the specimens exposed to Sc, Ss, and Scs, respectively. Thereafter, the load started to decrease with the depth inward from the corroded surface to the inner layer, where the load reached a stable level of approximately 4–5 mN for all specimens. The micro-mechanical property of the middle zone is higher than the other two layers, which is possibly due to the fact that the degree of hydration of this layer was higher compared to the inner layer. This in turn helped to densify the microstructure and reduce the porosity. Hence, the strength of this layer increased. Furthermore, it can also be noticed that the increase or decrease of the load in the specimen is a continuous process, indicating that the degradation of mortars is a gradual process and the boundary between layers is not easy to strictly define. As mentioned earlier, the three specimens started from almost similar loads in surface layer, which might be due to the fact that the micro-mechanical strength of the surface layer is lower because of the presence of epoxy resin. Hence, the surface mechanical strength of all specimens actually came from the original strength of the hardened epoxy resin. Afterwards, the strength

of the three specimens increased gradually, indicating the deterioration reductions of the binding matrix.
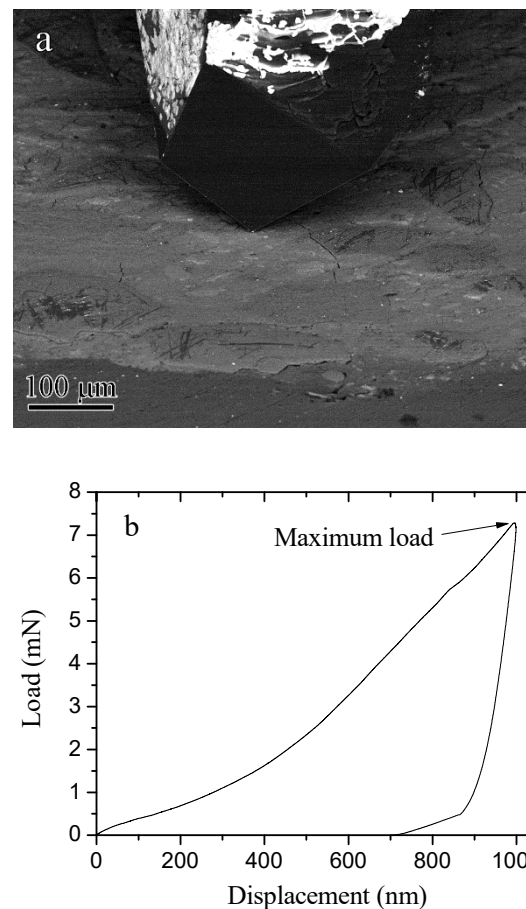

Figure 10. (**a**) BSE image of the indenter on the surface of mortar; (**b**) the load-displacement curve at a certain site.

For the middle layer, it is interesting to note that the peak load seems to follow a descending sequence, i.e., Sc > Ss > Scs. The peak load of specimen Sc is greater than that of specimen Ss due to the absence of gypsum in specimen Sc (Figure 11), which could significantly decrease the strength of this layer [38,39]. The lowest peak strength of specimen Scs can be explained by the crystallization pressure hypothesis [40], which states that the evaporation of liquid (such as during the drying process of the cyclic wetting and drying) could create supersaturation solutions of salts (such as NaCl or Na_2SO_4). Then, the crystals formed and grew in the pores, which exerted enough pressure to cause the damage of pore walls. Although specimen Scs has a similar chloride content to specimen Sc and a lower gypsum content than specimen Ss, the total quantity of chloride and sulfate ions was much greater than that in the specimens immersed in Sc or Ss. Thus, during the drying process, more crystals precipitated from the solution and exerted more pressure and stress to the pore wall. As a result, for the specimen Scs, the cyclic drying and wetting process led to a significant reduction in the micro-mechanical strength of this layer.

In the inner layer of the three specimens, the loads continuously decreased and tended to reach a constant value of around 4 mN. This implies that although the chloride and sulfate ions have transported into this layer, the strength was not affected considerably, compared to the unaffected (unaltered) 'healthy' region.
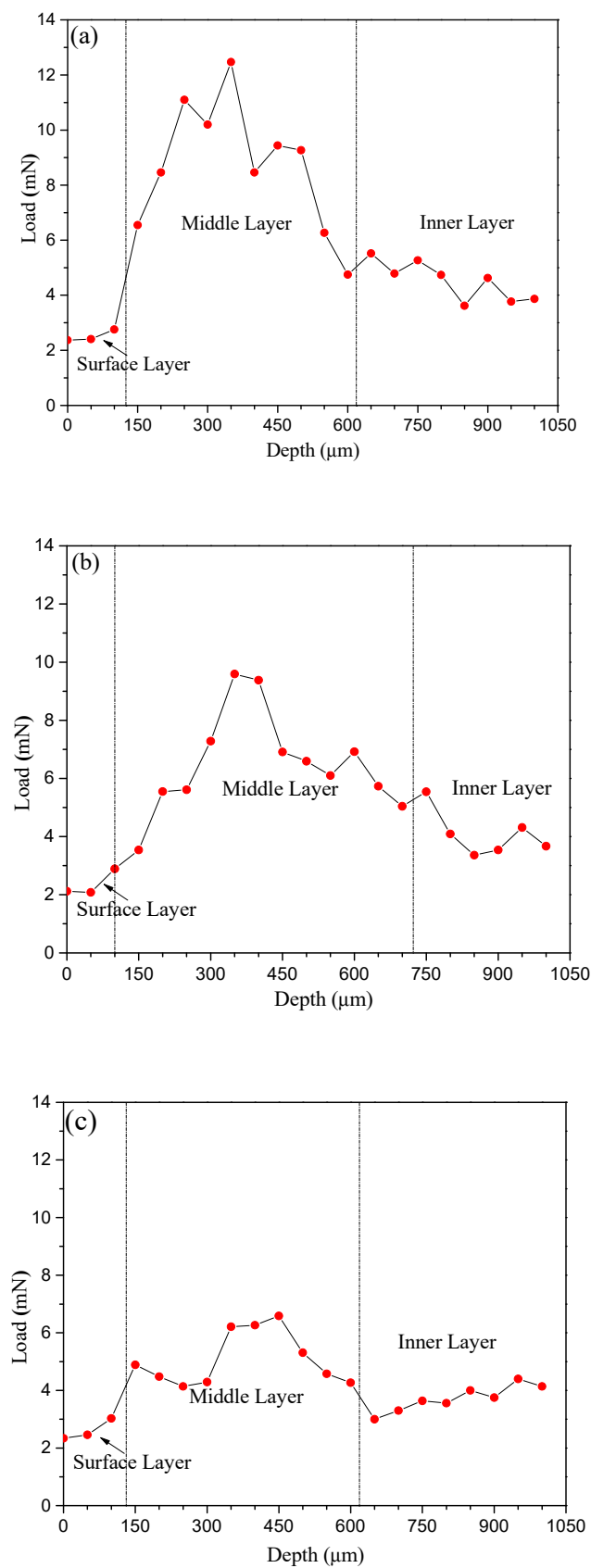
Figure 11. The maximum load along the transport direction from the surface to the inner part of specimens exposed to (**a**) Sc; (**b**) Ss, and (**c**) Scs. The three layers of each specimen are indicated by dotted lines in the plots and are consistent with the markings in Figure 11.

4. Conclusions

In this study, the synergistic effects of sulfate attack and chloride ingress on reinforced cement mortars under a cyclic drying–immersion condition were investigated through a non-destructive XCT technique and in situ nanoindentation testing. Based on the results, the following conclusions could be drawn:

(1). In terms of steel corrosion, chloride caused much more severe corrosion to steel than did the sulfate solution. For the specimen immersed in the combined solution (Scs), the existence of sulfate suppressed the steel corrosion caused by chloride. By investigating the damage on mortar cover, it was found that the sulfate caused much more damage to mortar covers than chloride did, likely due to the formation of expansive ettringite.

(2). After 24 drying–immersion cycles, the volume loss of specimens immersed in the sulfate solution were the highest (~7.1%), followed by those for the specimens exposed to the combined chloride and sulfate solution Scs (~6.3%), indicating that the presence of chloride suppressed the sulfate attack although this effect was not significant. The lowest volume loss of specimens occurred when they were immersed in the chloride solution (~2.6%). The competitive nature of chloride and sulfate was confirmed based on both qualitative and quantitative analyses.

(3). The degradation of mortars was found to be a layer-dependent process. The mechanical properties of all specimens decreased in the sequence of surface layer, inner layer, then middle layer since the middle layer obtained the most compact microstructure. Moreover, the mechanical strength of the middle layer increased in the following sequence (Scs < Ss < Sc), indicating that the total ion concentration would affect the performance (such as strength) of a local area due to the more remarkable physical salt crystallization than to chemical reactions (such as the leaching effect, hydration rate, etc.). However, the final degradation rate indicated by the surface shedding and volume loss of specimens was still dominated by chemical attack. For the surface and inner layers, the corresponding micro-mechanical strength appeared not to be significantly influenced by external solutions.

References

1. Maes, M.; De Belie, N. Resistance of concrete and mortar against combined attack of chloride and sodium sulphate. *Cem. Concr. Compos.* **2014**, *53*, 59–72. [CrossRef]
2. Liu, G.J.; Zhang, Y.S.; Ni, Z.W.; Huang, R. Corrosion behavior of steel submitted to chloride and sulphate ions in simulated concrete pore solution. *Constr. Build. Mater.* **2016**, *115*, 1–5. [CrossRef]
3. Ying, G.G.; Song, C.; Ren, J.; Guo, S.-Y.; Nie, R.; Zhang, L. Mechanical and durability-related performance of graphene/epoxy resin and epoxy resin enhanced OPC mortar. *Constr. Build. Mater.* **2021**, *282*, 122644. [CrossRef]
4. Sun, H.; Wu, W.; Zhao, Y.; Lin, Y.; Xu, S.; Zhang, T.; Zhang, X.; Xing, F.; Ren, J. Mechanical and durability properties of blended OPC mortar modified by low-carbon belite (C2S) nanoparticles. *J. Clean. Prod.* **2021**, *305*, 127087. [CrossRef]

5. Hekal, E.E.; Kishar, E.; Mostafa, H. Magnesium sulfate attack on hardened blended cement pastes under different circumstances. *Cem. Concr. Res.* **2002**, *32*, 1421–1427. [CrossRef]

6. Liu, P.; Chen, Y.; Wang, W.; Yu, Z. Effect of physical and chemical sulfate attack on performance degradation of concrete under different conditions. *Chem. Phys. Lett.* **2020**, *745*, 137254. [CrossRef]

7. Sotiriadis, K.; Rakanta, E.; Mitzithra, M.E.; Batis, G.; Tsivilis, S. Influence of Sulfates on Chloride Diffusion and Chloride-Induced Reinforcement Corrosion in Limestone Cement Materials at Low Temperature. *J. Mater. Civ. Eng.* **2017**, *29*, 12. [CrossRef]

8. Zuquan, J.; Wei, S.; Yunsheng, Z.; Jinyang, J.; Jianzhong, L. Interaction between sulfate and chloride solution attack of concretes with and without fly ash. *Cem. Concr. Res.* **2007**, *37*, 1223–1232. [CrossRef]

9. Chen, Z.; Wu, L.Y.; Bindiganavile, V.; Yi, C.F. Coupled models to describe the combined diffusion-reaction behaviour of chloride and sulphate ions in cement-based systems. *Constr. Build. Mater.* **2020**, *243*, 13. [CrossRef]

10. Xu, F.; Yang, Z.Q.; Liu, W.Q.; Wang, S.G.; Zhang, H.G. Experimental investigation on the effect of sulfate attack on chloride diffusivity of cracked concrete subjected to composite solution. *Constr. Build. Mater.* **2020**, *237*, 9. [CrossRef]

11. Douglas Hooton, R. Current developments and future needs in standards for cementitious materials. *Cem. Concr. Res.* **2015**, *78*, 165–177. [CrossRef]

12. Harrison, W.H. Effect of chloride in mix ingredients on sulphate resistance of concrete. *Mag. Concr. Res.* **1990**, *42*, 113–126. [CrossRef]

13. Maslehuddin, M.; Page, C.L.; Rasheeduzzafar. Temperature effect on the pore solution chemistry in contaminated cements. *Mag. Concr. Res.* **1997**, *49*, 5–14. [CrossRef]

14. Zhao, G.W.; Li, J.P.; Shi, M.; Cui, J.F.; Xie, F. Degradation of cast-in-situ concrete subjected to sulphate-chloride combined attack. *Constr. Build. Mater.* **2020**, *241*, 10. [CrossRef]

15. Zhutovsky, S.; Kovler, K. Effect of internal curing on durability-related properties of high performance concrete. *Cem. Concr. Res.* **2012**, *42*, 20–26. [CrossRef]

16. Alkaysi, M.; El-Tawil, S.; Liu, Z.C.; Hansen, W. Effects of silica powder and cement type on durability of ultra high performance concrete (UHPC). *Cem. Concr. Compos.* **2016**, *66*, 47–56. [CrossRef]

17. Li, Y.L.; Zhao, X.L.; Raman, R.K.S. Mechanical properties of seawater and sea sand concrete-filled FRP tubes in artificial seawater. *Constr. Build. Mater.* **2018**, *191*, 977–993. [CrossRef]

18. Zhou, Z.D.; Qiao, P.Z. Durability of ultra-high performance concrete in tension under cold weather conditions. *Cem. Concr. Compos.* **2018**, *94*, 94–106. [CrossRef]

19. Myers, R.J.; Bernal, S.A.; Nicolas, R.S.; Provis, J.L. Generalized Structural Description of Calcium–Sodium Aluminosilicate Hydrate Gels: The Cross-Linked Substituted Tobermorite Model. *Langmuir* **2013**, *29*, 5294–5306. [CrossRef]

20. Itty, P.A.; Serdar, M.; Meral, C.; Parkinson, D.; MacDowell, A.A.; Bjegovic, D.; Monteiro, P.J.M. In situ 3D monitoring of corrosion on carbon steel and ferritic stainless steel embedded in cement paste. *Corros. Sci.* **2014**, *83*, 409–418. [CrossRef]

21. Xi, X.; Yang, S.T. Investigating the spatial development of corrosion of corner-located steel bar in concrete by X-ray computed tomography. *Constr. Build. Mater.* **2019**, *221*, 177–189. [CrossRef]

22. Zhou, Y.W.; Zheng, B.W.; Sui, L.L.; Xing, F.; Li, P.D.; Sun, H.F. Effects of external confinement on steel reinforcement corrosion products monitored by X-ray microcomputer tomography. *Constr. Build. Mater.* **2019**, *222*, 531–543. [CrossRef]

23. Gautham, S.; Sindu, B.S.; Sasmal, S. Evaluation of the phase properties of hydrating cement composite using simulated nanoindentation technique. *Model. Simul. Mater. Sci. Eng.* **2017**, *25*, 22. [CrossRef]

24. Constantinides, G.; Ulm, F.J. The effect of two types of C-S-H on the elasticity of cement-based materials: Results from nanoindentation and micromechanical modeling. *Cem. Concr. Res.* **2004**, *34*, 67–80. [CrossRef]

25. Kumar, V. Protection of steel reinforcement for concrete—A review. *Corros. Rev.* **1998**, *16*, 317–358. [CrossRef]

26. Sorelli, L.; Constantinides, G.; Ulm, F.J.; Toutlemonde, F. The nano-mechanical signature of Ultra High Performance Concrete by statistical nanoindentation techniques. *Cem. Concr. Res.* **2008**, *38*, 1447–1456. [CrossRef]

27. Moser, R.D.; Allison, P.G.; Chandler, M.Q. Characterization of Impact Damage in Ultra-High Performance Concrete Using Spatially Correlated Nanoindentation/SEM/EDX. *J. Mater. Eng. Perform.* **2013**, *22*, 3902–3908. [CrossRef]

28. Cheng, S.; Shui, Z.; Gao, X.; Yu, R.; Sun, T.; Guo, C.; Huang, Y. Degradation mechanisms of Portland cement mortar under seawater attack and drying-immersion cycles. *Constr. Build. Mater.* **2020**, *230*, 116934. [CrossRef]

29. Zhang, X.; Jiang, C.; Chen, Y.; Yuan, B.; Memon, S.A.; Ren, J.; Xing, F.; Sun, H. Influence of initial defects on the degradation of steel reinforced mortar exposed to cyclic wetting and drying environment based on 3D scanning. *Constr. Build. Mater.* **2022**, *325*, 126591. [CrossRef]

30. Ren, J.; Guo, S.; Su, J.; Zhao, T.; Chen, J.; Zhang, S. A novel TiO_2/Epoxy resin composited geopolymer with great durability in wetting-drying and phosphoric acid solution. *J. Clean. Prod.* **2019**, *227*, 849–860. [CrossRef]

31. Chen, Y.; Gao, J.; Tang, L.; Li, X. Resistance of concrete against combined attack of chloride and sulfate under drying–wetting cycles. *Constr. Build. Mater.* **2016**, *106*, 650–658. [CrossRef]

32. Sun, H.; Liu, S.; Cao, K.; Yu, D.; Memon, S.A.; Liu, W.; Zhang, X.; Xing, F.; Zhao, D. Degradation mechanism of cement mortar exposed to combined sulfate–chloride attack under cyclic wetting–drying condition. *Mater. Struct.* **2021**, *54*, 138. [CrossRef]

33. *Gb/t3274-2017*; Hot-Rolled Plates and Strips of Carbon Structural Steels and High Strength Low Alloy Structural Steels. Standards Press of China: Beijing, China, 2017.

34. *Gb/t17671-1999*; Method of Testing Cements—Determination of Strength. Chinese Standards Institute: Beijing, China, 1999.

35. Sun, H.; Liu, S.; Yu, F.; Zhang, X.; Wu, C.; Xing, F.; Ren, J. Behaviour of cement binder exposed to semi-immersion in chloride-rich salt solutions and seawater with different RH levels. *Cem. Concr. Compos.* **2022**, *131*, 104606. [CrossRef]
36. Zhang, M.H.; Chen, J.K.; Lv, Y.F.; Wang, D.J.; Ye, J. Study on the expansion of concrete under attack of sulfate and sulfate-chloride ions. *Constr. Build. Mater.* **2013**, *39*, 26–32. [CrossRef]
37. Luo, S.; Zhao, M.; Jiang, Z.; Liu, S.; Yang, L.; Mao, Y.; Pan, C. Microwave preparation and carbonation properties of low-carbon cement. *Constr. Build. Mater.* **2022**, *320*, 126239. [CrossRef]
38. Glasser, F.P.; Marchand, J.; Samson, E. Durability of concrete—Degradation phenomena involving detrimental chemical reactions. *Cem. Concr. Res.* **2008**, *38*, 226–246. [CrossRef]
39. Cohen, M.D.; Mather, B. Sulfate Attack on Concrete—Research Needs. *Aci. Mater. J.* **1991**, *88*, 62–69.
40. Thaulow, N.; Sahu, S. Mechanism of concrete deterioration due to salt crystallization. *Mater. Charact.* **2004**, *53*, 123–127. [CrossRef]